Structure, Seebeck coefficient and DC electrical conductivity of $Bi_2Mn_4O_{10}$ prepared by mechanochemical method

Shereef A. Fareed[1],* , Makram Ibrahim[1], Ahmed E. Hannora[2], and M. M. El-Desoky[3]

[1] Solar and Space Research Department, National Research Institute of Astronomy and Geophysics (NRIAG), Helwan 11421, Cairo, Egypt

[2] Department of Sciences and Engineering Mathematics, Faculty of Petroleum and Mining Engineering, Suez University, Suez 4351, Egypt

[3] Department of Physics, Faculty of Science, Suez University, Suez 43518, Egypt

ABSTRACT

Bismuth and manganese oxides were mixed as source-materials using the mechanochemical technique followed by heat treatment to prepare the phase $Bi_2Mn_4O_{10}$. The X-Ray Diffraction (XRD) analysis was carried out to obtain the formed phases during the mechanochemical process. Bismuth manganese oxide phase with the chemical formula $Bi_2Mn_4O_{10}$ was formed at heat treatment 1073 K and was partially decomposed to γ-$Bi_{12.8}O_{19.2}$ and α-Mn_2O_3 after 5 h of milling time. The variation of the crystallite size is obtained at different milling time (1 h, 5 h, 10 h, 15 h, 30 h and 50 h). The temperature dependency of the DC electrical conductivity was observed at different milling times in the temperature range 300–425 K for the samples milled at 5 h, 10 h, 30 h and 50 h. The temperature dependency (300–4 80 K) of the thermoelectric power/Seebeck coefficient (S) and its modulus variation with milling time were observed; the modulus varied in the range (45 μV/K-277 μV/K). The concentration of manganese ions (N), the average distance between manganese ions (R) and the fraction (C) of reduced transition ions were calculated for all samples. The hopping carrier mobility (μ) of the samples was also calculated at a fixed temperature. As a result, the conduction mechanism agreed with the non-adiabatic process of small polaron hopping.

Address correspondence to E-mail: shereefscience@gmail.com

1 Introduction

The combinational properties of multiferroic materials are considered the main key for the importance of their widely found applications such as energy transducers [1] and battery electrodes [2]. Generally, the perovskite manganite is one of the promising multiferroic materials due to its giant magneto-resistance, these materials formed in the orthorhombic crystal structure. Haiou Wang and others investigated the magnetic parameters of samarium calcium manganite ($Sm_{0.5}Ca_{0.5}MnO_3$), they prepared it by high-temperature solid-state reaction [3], they studied the effect of milling time on the crystallite size and measured the magnetic hysteresis loop of the sample as well as the temperature dependency of the magnetization. In another investigation, the magnetization, magneto-resistance and elastic properties were obtained for some manganite materials $Sm_{0.56}(Sr_{0.44-x}Me_x)—MnO_3$ (Me = Ba, Cd, Ca) at different molar ratios [4], The total magnetic moment in bismuth manganite is weak relatively with many samples of bismuth oxides such as $Bi_{25}Fe_{39}$ [5]. Structure magnetic, dielectric and magneto-dielectric properties were obtained for other samples such as $BaFe_{12-x}Ti_xO_{19}$ [6, 7]. Recently, a large spontaneous polarization and multiferroic properties were discovered at room temperature in doped M-type hexaferrites [8, 9]. The electrical, magnetic and magneto-dielectric properties can be changed under the influence of structural parameters such as oxygen stoichiometry, crystallite size and structure distortion caused by specifying the dopant ionic radii and concentration [10, 11]. In a previous study [12], they showed that the dopant concentration for $Bi_{1-x}Ba_x$-$Fe_{1-x}Ti_xO_3$ drives the structural transition from rhombohedral polar phase to a cubic phase and extended in the range $0.20 \le x \le 0.35$ to polar active pseudo-cubic phase. There are different methods for preparing the perovskite structure and its derivatives such as sol–gel, acorus calamus and solid-state reaction [13–15]. The perovskite $BiMnO_3$ phase was previously obtained after the amorphization of the constituent oxides [16]. Preparation of the perovskite structure $BiMnO_3$ by solid-state reaction required high pressure and high temperature [17, 18]. The orthorhombic crystal structure of $Bi_2Mn_4O_{10}$ belongs to a group of mullite-type compounds which have multiferroic properties at low temperatures [19, 20]. In mechanochemical preparation method, The powder particles during milling trapped between the colliding balls undergo deformation and/or fracture processes [21–23]. Multiferroic materials have a magneto-electric behavior and exhibit ferro/antiferromagnetic and ferroelectric properties at the same time [24]. The unpaired electrons and the orbital ordering of Manganese cations are responsible for the coexistence of both ferromagnetic and ferroelectric properties [25]. The Curie temperature of the bismuth Manganite has a value of about 105 K and it exhibits ferroelectricity at the same time after Tc = 100 K [26, 27]. The electrical conductivity and Seebeck coefficient are also important parameters to electrically characterize many materials; in a study, the two quantities were analyzed for multiple-filled X–$CoSb_3$ skutterudites (X = Yb, Ca, Ba, Al, Ga, In, La, Eu) from 300 to 823 K [28]. In the current study, bismuth manganese oxide with the formula $Bi_2Mn_4O_{10}$ was formed after heat treatment at 1073 K according to $Bi_2O_3 + 2\ Mn_2O_3 + 0.5\ O_2 \rightarrow Bi_2Mn_4O_{10}$. The cubic unit cell of the perovskite structure (ABO_3) was distorted into an orthorhombic structure with space group (Pbam) and two sites octahedral and pyramidal [25, 29, 30]. $Bi_2Mn_4O_{10}$ was previously formed using a high energetic milling machine [15]. Mechanochemical synthesis or solid-state reaction technique was selected for samples preparation. In this study, we focused on the investigation of the thermoelectric behavior and temperature dependency of the DC conductivity. The conductivity in nanostructured materials that contain a large amount of transition metal ions (TMO) is described by the small polaron hopping (SPH) mechanism between such ions [31, 32]. The carrier concentration (C) is related to the concentration of TMO in multivalence states [33–36]. Thermoelectric power or Seebeck coefficient (S) is significantly large for the nanostructured materials that contain large amounts of TMO which is required for many different applications. Generally, Heike's formula [33] can be applied to evaluate the S and C values. The phase $Bi_2Mn_4O_{10}$ has been investigated previously as an anode material f or advanced Li-ion battery systems [36, 37].

2 Experimental work

There are several methods for preparing our samples [13–15] but in this study, we selected the solid-state reaction where high purity oxides of bismuth (Bi_2O_3)

and manganese (MnO_2) (Aldrich 99%) were mixed using a stainless-steel vertical ball mill attritor for different milling times at 500 rpm. The prepared samples were pressed at 5 tons into a pellet with a 12 mm diameter using a uniaxial press. The pressed powder samples were heat-treated at 873 K for 2 h with calcination at 1073 K for 5 h in the open atmosphere. The XRD patterns were carried out using "SIEMENS D5000" X-ray diffractometer with target CuKα radiation. The structure was also studied by high-resolution transmission electron microscope "HRTEM" using "JEOL 2100 HRT". We investigated the variation of the DC electrical behavior of the samples with temperature as shown in Fig. 1, the temperature dependent DC conductivity was calculated from the measured resistance using the "Keithley 197" multi-meter, where K-type thermocouple was connected to a digital thermometer to measure the temperature gradient in a non-inductive controllable electric furnace. The thermoelectric power or Seebeck coefficient was measured using the setup as shown in Fig. 2 where two identical heaters with their accompanying K-type digital thermometers were used to raise the temperature at the two sides of the sample with a difference of ΔT, the induced voltage measured by multi-meter "Agilent 34401A". The used sample cell with the two identical heaters is homemade while the measuring devices were connected to a computer just to read data and export it in an excel sheet.
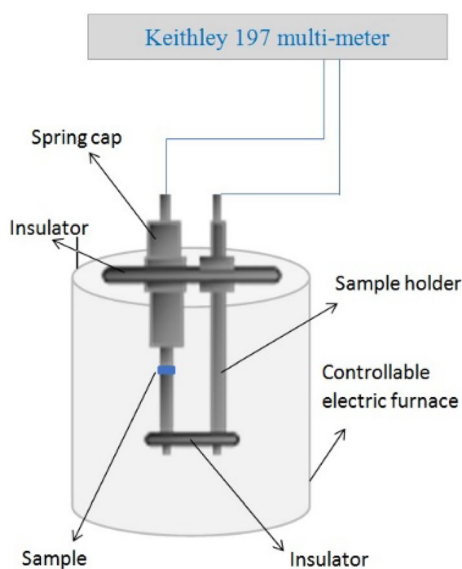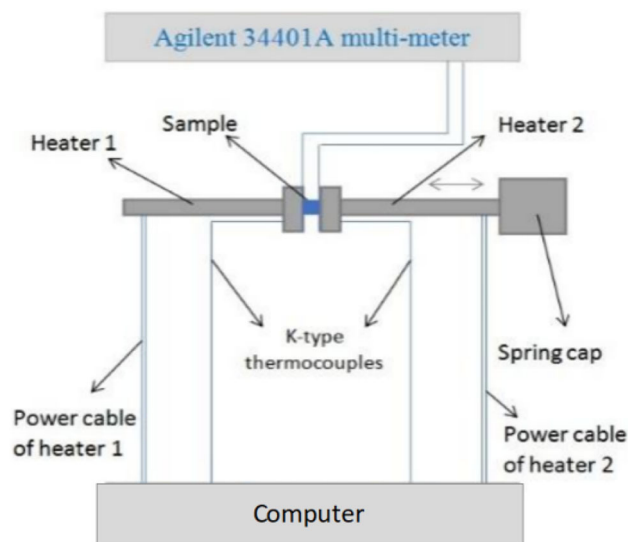

Fig. 1 DC conductivity measurement setup

Fig. 2 Thermoelectric power measurement setup

3 Results and discussion

3.1 Structure

Figure 3a shows X-ray diffraction patterns of mechanochemical process where fully crystalline bismuth and manganese oxide phases transformed to non-crystalline phase. After 5 h of mechanical treatment several peaks diapered. The intensity of the residual peaks decreases while, the full width at half-maximum increases. The fine structure formed after 5 h directly transformed to non-crystalline phase after 10 h. The mechanical treatment extended to 50 h to ensure a full amorphization conversion and/or recrystallization process. After 50 h of mechanical treatment, the sample shows only non-crystalline phase formation. Figure 3b shows the XRD patterns of six samples prepared by the mechanochemical reaction; each of them is milled for a different specific time. All samples as mentioned above were heat-treated at the same temperature (1037 K). The XRD showed the spectra of the heat-treated samples at different milling time with different highest peak broadening; this is due to the variation of the crystallite size and micro-strain. After 1 h of treatment, the broadest crystalline peaks appeared and then became slightly and relatively sharp at 5–50 h milling time.

According to the XRD spectra and the semi-quantitative analysis using PANalytiacl X'Pert HighScore plus software listed in Table 1, the bismuth manganese oxide phase with chemical formulas
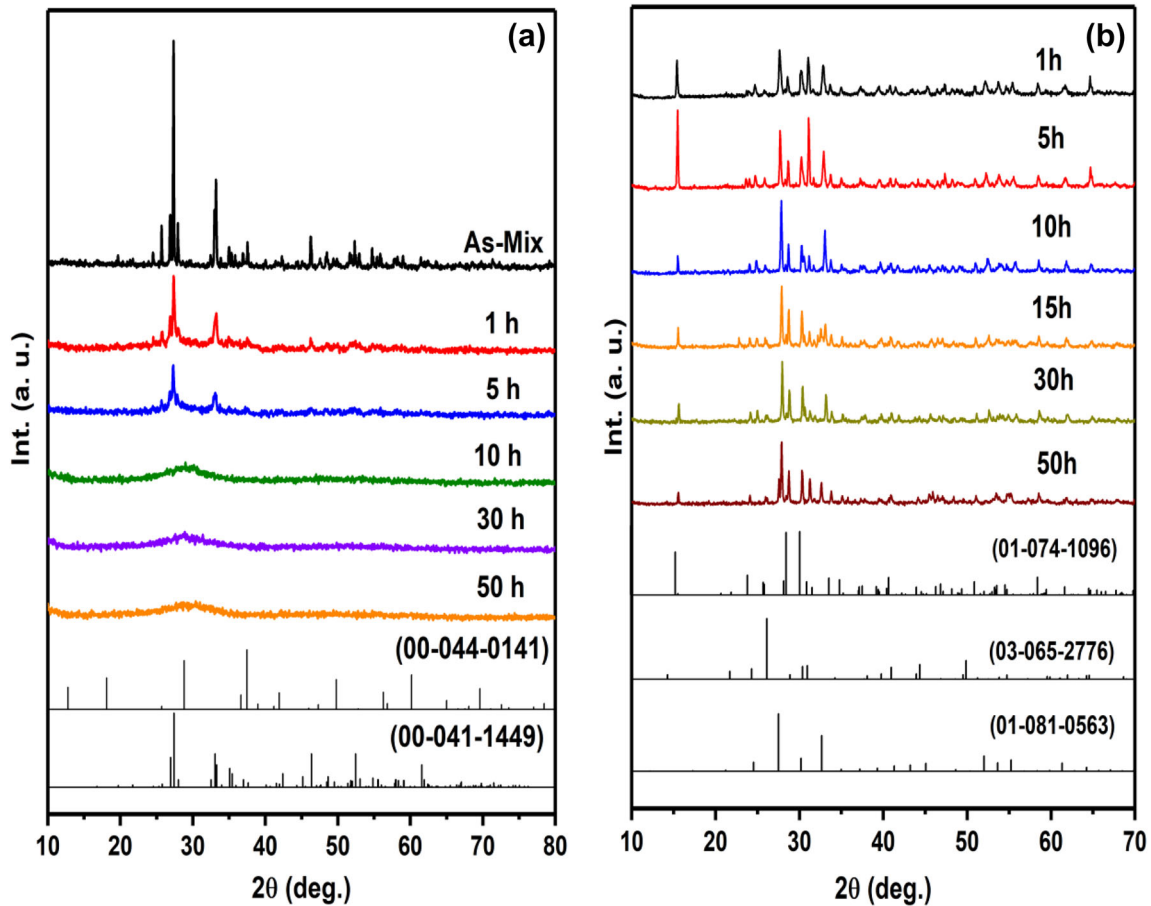
Fig. 3 XRD patterns of **a** mechanical treatment and **b** heat treated samples at 1037 K

Table 1 Quantitative analysis, crystallite size and micro-strain of heat-treated samples at 1073 K for 5 h

Mechanical treatment time (h)	1	5	10	15	30	50
$Bi_2Mn_4O_{10}$ (%)	81	88	66	68	36	39
α-Mn_3O_4 (%)	7	7	9	8	10	11
γ-$Bi_{12.8}O_{19.2}$ (%)	12	5	25	24	54	50
Average crystallite size D(nm)	47.6	58.1	110.3	95.7	94.6	102
Micro-strain (%)	0.078	0.11	0.21	0.136	0.146	0.21

$Bi_2Mn_4O_{10}$ was formed after 5 h of heat-treatment at 1073 K with 12% secondary phases of α-Mn_2O_3 and γ-$Bi_{12.8}O_{19.2}$, this was confirmed from the corresponding ICCD cards (01-074-1096), (03-065-2776) and (01-081-0563), respectively. $Bi_2Mn_4O_{10}$ has an orthorhombic crystal structure with space group Pbam (No. 55).

The orthorhombic phase showed (001) preferred orientation at 1 h and 5 h heat-treated samples. By increasing the time of milling, the percentage of the amount of Mn_3O_4 and $Bi_{12.8}O_{19.2}$ became larger where Mn_3O_4 is a tetragonal phase with space group I41/amd (No. 141) while $Bi_{12.8}O_{19.2}$ is a cubic system with space group I23 (No. 197). It is clear from Table 1 that the percentage of the orthorhombic phase formation of $Bi_2Mn_4O_{10}$ is the largest percentage at 5 h of milling time and relatively, the other samples have lower percentages due to the decomposition of $Bi_2Mn_4O_{10}$ to α-Bi_2O_3 and α-Mn_2O_3 [14]. Also, $BiMn_2O_5$ has a structure, which contains octahedral-coordinated Mn^{4+}ions and Mn^{3+}ions located in square pyramids [35]. The formed phases and variation of the crystallite size and micro-strain are listed in Table 1. Each sample owned different percentages of

the formed phases, which is why the binding distance, oxygen stoichiometry and cation distribution are different at each milling time. This also reflects the interpretation of the changes in the unit cell volume and concentration of manganese ions "N", consequently, the exchange interaction and the resultant electric and magnetic properties will be influenced. The effect of oxygen stoichiometry of some manganites on the magnetic and electric properties is reported by S.V. Trukhanov and others [38–41]. The crystallite size (D) and micro-strains (ε) of the mechanical milled sample can be estimated from the full width at half maximum of the major peaks (β). Hall-Williamson relation was used to separate these factors as given in Eq. (1):

$$\beta \cos\theta = \frac{k\lambda}{D} + 4\varepsilon \tag{1}$$

where, (θ) is the Bragg angle, λ is the wavelength and k is the Scherrer constant (shape factor) usually from 0.8 to 1.

The micro-strains estimated by the Hall-Williamson relation varied from 0.078 (%) to 0.210 (%) with crystallite sizes ranging from 47.6 nm to 110 nm. Usually, the reaction during mechanical treatment is related to the strain generated in the samples which enhances the destabilization of the crystal structure. On the other hand, the variation of the crystallite size could be attributed to the phase change with milling time during the diffusion process and agglomeration so the different percentages of the three formed phases play a role in this variation. Its reported previously that the change in the structure may lead to such variation in the crystallite size with milling time [42]. The variation of lattice parameters as a function of milling time is illustrated in Table 2.

Figure 4a–c shows the TEM images of the prepared samples after milling times of 5 h, 10 h and 50 h and heat treatment at 1073 K. At each milling time we have three images; from left to right, the images represent the crystallite size in different grains, the d-spacing within the crystals and the diffraction pattern. The concentric circles in the diffraction pattern and spots confirmed the polycrystallinity of the prepared samples. In addition, the appeared multigrains confirmed the polycrystalline structure.

The average crystallite size at a magnification scale of 50 nm was measured for each sample. It's clear from Fig. 4a that the sample at 5 h milling time is comparatively own the smallest crystallite size with

Table 2 Variation of lattice parameters as a function of milling time at constant heat treatment temperature (1073 K for 5 h)

Phase	a	b	c	Note
$Bi_2Mn_4O_{10}$	7.52	8.53	5.77	1 h
	7.51	8.53	5.77	5 h
	7.54	8.53	5.69	10 h
	7.46	8.53	5.76	30 h
	7.48	8.53	5.76	50 h
	7.54	8.53	5.77	ICCD (01–074-1096)
$\gamma\text{-}Bi_{12.8}O_{19.2}$	10.19			1 h
	10.18			5 h
	10.14			10 h
	10.09			30 h
	10.26			50 h
	10.23			ICCD (01–081-0563)

the average value 54 nm which is slightly closed to that calculated from XRD (58 nm). The d-spacing was also measured (d = 0.27 nm), in this sample as reported from XRD spectra, phase $Bi_2Mn_4O_{10}$ was formed with 88% relative to the other samples. In Fig. 4b, c, the TEM graphs of the multi-phase samples at milling times of 10 h and 50 h appeared as a polycrystalline structure and have average crystallite sizes of 108 nm and 101 nm with d-spacing of 0.24 nm and 0.29 nm, respectively.

3.2 Thermoelectric power and DC conductivity

We measured the thermoelectric power versus temperature for the prepared samples at the milling time of 5 h, 10 h, 30 h and 50 h, the results are shown in Fig. 5 where the negative value of the Seebeck coefficient indicates n-type conductivity.

The obvious variation of |S| with temperature (300–480 K) is backed to the small-polaron conduction mechanism with reducing the concentration of the Mn^{3+} ions [43]. The sample with milling time of 5 h which had the highest percentage of the phase formation of $Bi_2Mn_4O_{10}$ owns the maximum value of |S| (277 μV/K) at 480 K, this is ascribed to the ferroelectricity of the sample where the orientation of the electric dipole moments increase the induced voltage during heat transfer. The variation of |S| for prepared samples is shown in Fig. 6. Seebeck coefficient was used to determine the concentration ratio
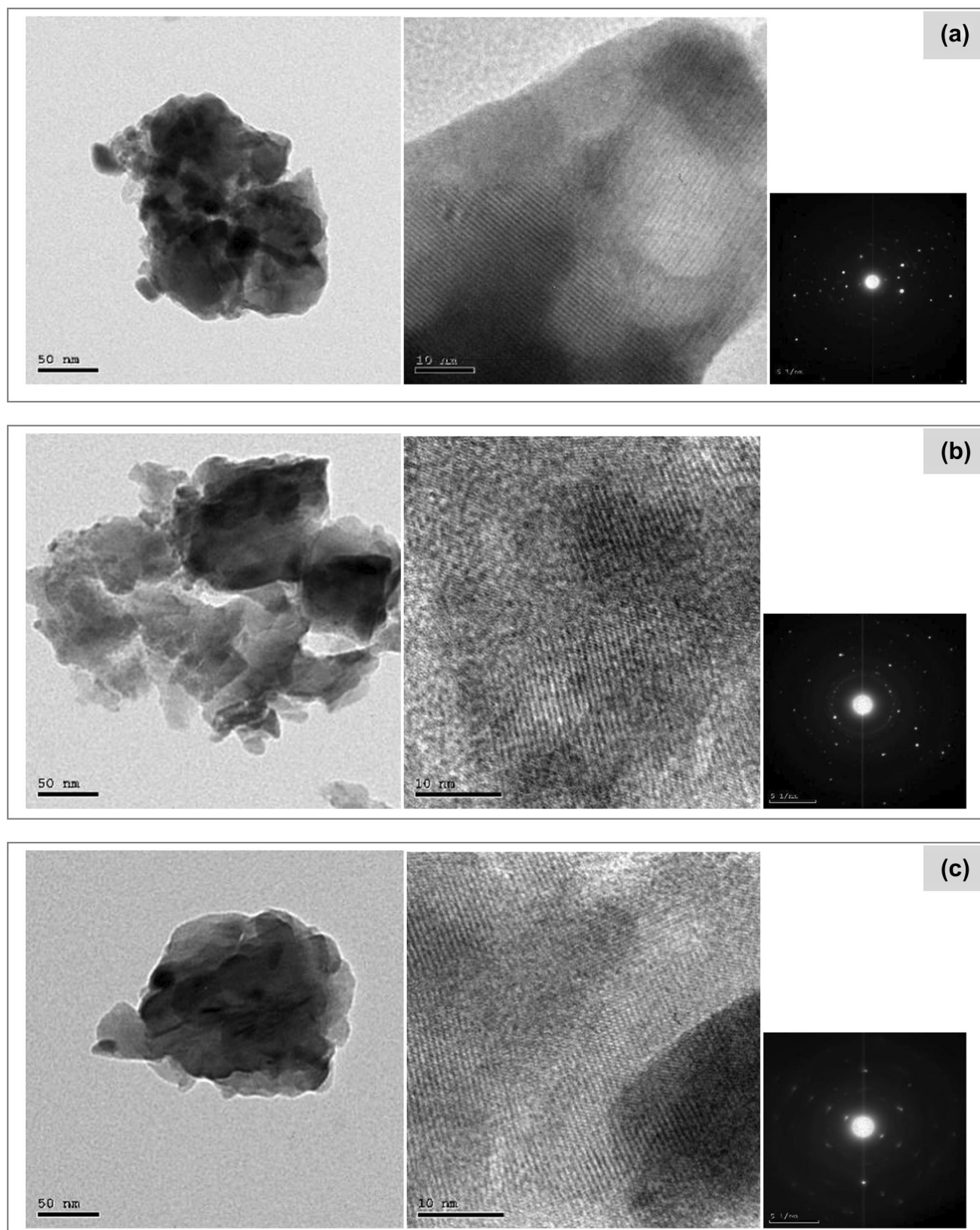
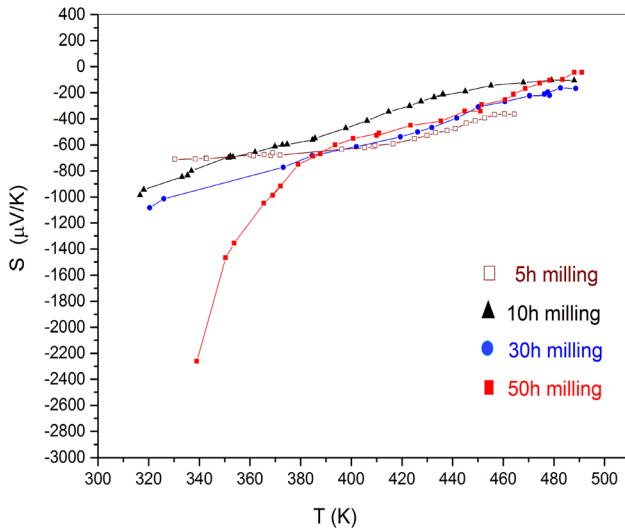**Fig. 4** TEM of prepared samples heated at 1073 K with milling time at 5 h (**a**), 10 h (**b**) and 50 h (**c**)

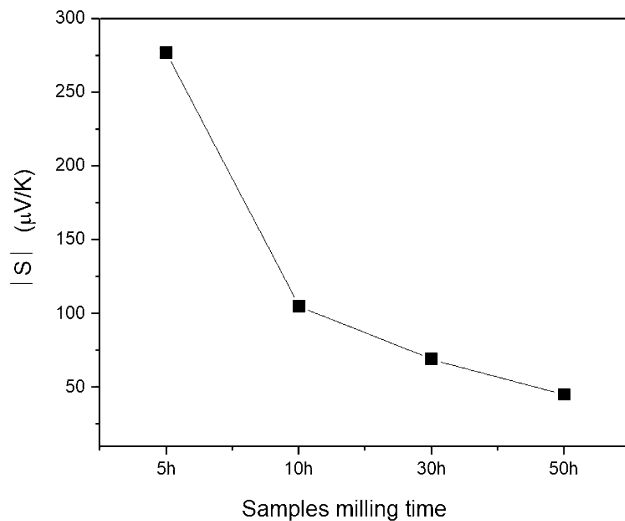**Fig. 5** Seebeck coefficient of the heat-treated samples at 1073 K with different milling time

Fig. 7 DC conductivity of heat-treated samples with different milling time

Fig. 6 Variation of absolute value of Seebeck coefficient with milling time for the samples at 480 K

Fig. 8 Logarithmic DC conductivity of heat-treated samples with different milling time

(C) from temperature-independent Heike relation given in Eq. 2:

$$S = \frac{k}{e}\left[\ln\left(\frac{C}{1-C}\right) + A\right] \tag{2}$$

A is neglected for small polaron hopping conductors. The ratio of the concentration of reduced transition metal is varied from 0.15 to 0.26.

The electrical properties of the prepared samples were investigated at different temperature degrees; Fig. 7 shows the measured DC conductivity and its variation with temperature for all samples while Fig. 8 shows the logarithmic DC conductivity
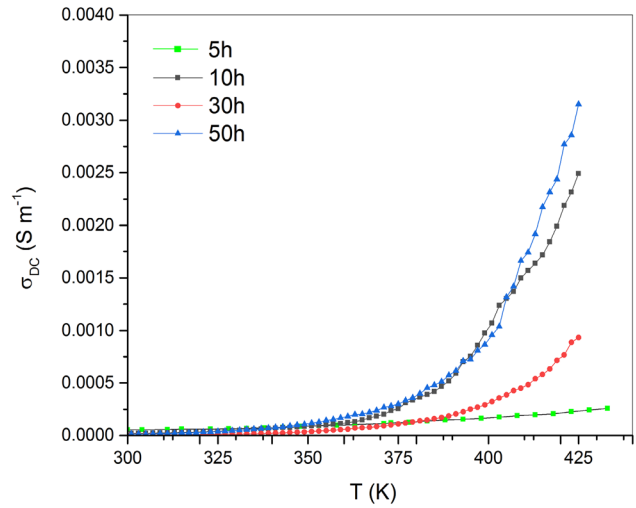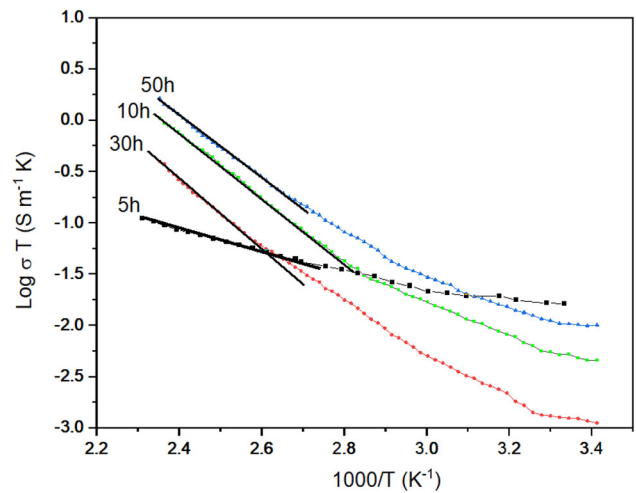
multiplied by applied temperature against the reciprocal of temperature ($1/T$) for the prepared samples milled at 5 h, 10 h, 30 h and 50 h.

All the samples have a multi-phase structure as mentioned in Table 1 except the sample prepared at 5 h of milling time which is belonging to the phase $Bi_2Mn_4O_{10}$ by 88%. The Arrhenius Mott formula can be used to describe the behavior of DC conductivity:

$$\sigma = \sigma_0 exp(-W/kT) \tag{3}$$

where W is the activation energy, k is the Boltzmann constant and σ_0 is a pre-exponential factor.

Table 3 Some physical properties of the prepared samples

Milling time (h)	5	10	30	50
Debye temperature θ_D(K)	740	706	770	738
Molar volume V_m(cm^3/mol)	40.08	34.80	34.68	38.98
Density ρ (gm/cm^3)	7.78	8.960	8.990	8.000
No. of manganese ions N($\times 10^{22}$) (cm^{-3})	1.5026	1.7305	1.7363	1.5451
Average distance between ions R(nm)	0.653	0.623	0.622	0.647
Optical phonon frequency ν_0 ($\times 10^{13}$)	0.7706	0.735	0.802	0.766

Table 3 shows some physical properties for all samples including Debye temperature (θ_D), experimental density (ρ), molar volum (V_m), number of transport ions (N), average distance between ions (R) and optical phonon frequency (ν_0), we obtained θ_D to calculate the Activation Energy (W) and according to Eq. 3 we calculated the logarithmic value of the DC conductivity as shown in Fig. 8.

The variation trend of the logarithmic conductivity of the sample milled at 5 h is different from the other samples, this is referred to the fact revealed from XRD; that the formation percentage of $Bi_2Mn_4O_{10}$ in the multi-phase samples which milled at 10 h, 30 h and 50 h is varied from 36 to 66% with 25% to 54% of $Bi_{12.8}O_{19.2}$ while at 5 h, the formation percentage of $Bi_2Mn_4O_{10}$ was 88% with only 5% of $Bi_{12.8}O_{19.2}$ phase. The experimental density varied from 7.78 to 8.99 gm/cm^3, generally this variation referred to the deferent formed phases in each sample where the relative ionic radii of the constituents control the interstitial volume and play the main role in the variation of density and porosity. The activation energy is affected by the unit cell volume which varied according to the difference in the formed phases. From a study [44], the activation energy is directly proportional to the unit cell volume in a manganite sample. The behavior of the logarithmic conductivity represents the Arrhenius plot between 300 and 454 K. The deviation from linearity (at a high-temperature regime) occurred around θ_D/2 (from 353 to 454 K depending on milling time). The corresponding values of Debye temperature θ_D at the end of the linear dependency of the DC conductivity varied from 706 to 770 K as given in Table 3. The linearity after θ_D is not best preserved which indicates small polaron hopping (SPH) [45]. We measured the density to calculate the number of transition metal ion sites per unit volume (N) using the following equation:

$$N = \rho N_A \left[\frac{Mole percent of composition}{Average molecular weight of compoition} \right] \quad (4)$$

where (N_A) is the Avogadro's number and ρ is the sample density which experimentally measured from Archimedes principle using toluene liquid as an immersing medium with density 0.8669 g/cm^3.

The average distance between manganese ions (R) is related to number of sites per unit volume by the relation given in Eq. 5:

$$R = \left(\frac{4\pi N}{3} \right)^{-\frac{1}{3}} \quad (5)$$

Another purpose of Debye temperature θ_D is to obtain the optical phonon frequency (ν_o) using Eq. 6 [46, 47]:

$$\nu_o = \frac{k\theta_D}{h} \quad (6)$$

where k is the Boltzmann constant and h is Planck constant.

All the above parameters are needed to identify the conduction mechanism through the adiabatic or non-adiabatic regime. In non-adiabatic approximation, the DC conductivity for the hopping polarons proposed by Austin and Mott [48–50] as given in Eq. 7:

$$\sigma = C(1 - C) \times \frac{\nu_0 N e^2 R^2}{kT} \exp(-2\alpha R) \exp\left(-\frac{W}{kT} \right) \quad (7)$$

For adiabatic approximation, the term exp (-αR) is neglected and the conductivity is given by:

$$\sigma = C(1 - C) \times \frac{\nu_0 N e^2 R^2}{kT} \exp\left(-\frac{W}{kT} \right) \quad (8)$$

where (α) is the electron-wave function decay constant (tunneling factor), (c) is the ratio of the ion concentration in the low valence state to the total concentration of the transition metal ions.

At a fixed temperature, it is easy to estimate the nature of polaron hopping, adiabatic or non-adiabatic by plotting activation energy against the logarithm of the conductivity. By calculating the slope and interception as illustrated in Fig. 9, the resultant
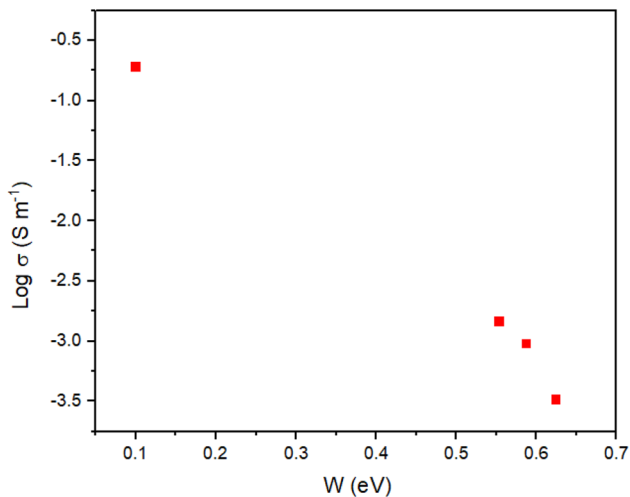
Fig. 9 Logarithmic DC conductivity variation of the heat-treated samples (1073 K) against activation energy in electron volt

temperature is $T = 539.6$ K. According to the above results, the conduction is due to non-adiabatic small polaron hopping of electrons because there is a big difference between the estimated temperature and the selected measured-temperature (401 K). Also, the effect of milling time on the pre-exponential factors (σ_o) obtained from the straight line fitting the data. The decrease of pre-exponential factors with milling time confirms again the non-adiabatic mechanism of the polaron hopping. Figure 10 illustrates the variation of activation energy and log σ with milling time at 401 K.

Thermoelectric power and conductivity measurements confirm the presence of a small number of

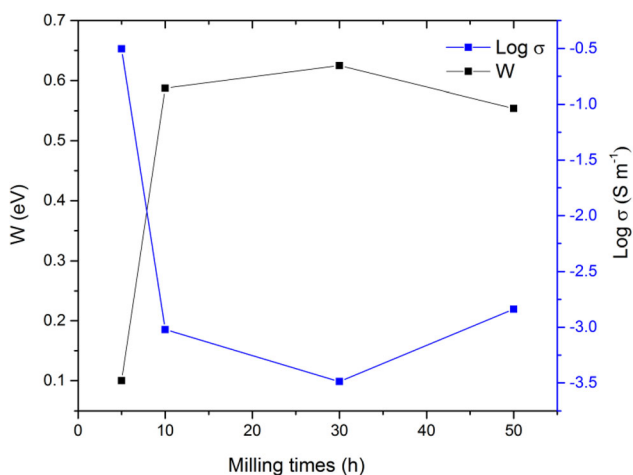**Fig. 10** Variation of activation energy and log σ with milling time at 401 K

electrons, due to incomplete oxidation of the sample. It is reported [45], that the perfectly stoichiometric manganite $CaMnO_3$ should not contain Mn^{3+} cations. In the n-type manganite, Mn^{4+} ions offer available sites for charge carriers, taking into account the spin state of the Mn^{4+} ions. With increasing temperature concentration of Mn^{3+} disproportionation increases which influences the charge carriers through forming Mn^{2+} and Mn^{4+} from $2Mn^{3+}$.

Oxygen addition/removal from the structure of the manganite plays a significant role in the electrical properties. The conduction occurred through small-polaron transport between Mn^{3+} and Mn^{4+} ions [51]. $BiMnO_3$ has activation energy value of 0.51 eV [52]. The measured activation energy for electrical conductivity in stoichiometric bismuth manganite $BiMnO_3$ yields a comparable value of 0.26 eV [53]. The present work activation energy values varied in the range of 0.1–0.63 eV depending on the milling time. The crystallite size is significantly affecting the $Mn - O - Mn$ bond length and bond angle. The deformation of the unit cell resulted from the mechanochemical treatment customizing the overlapping of O (p-orbitals) and Mn (d-orbitals). The double exchange mechanism takes a place at Mn^{3+}–O–Mn^{4+} electron-hopping conduction. As illustrated in Fig. 6, the modulus of Seebeck coefficient |S| increased from 108 μV/K to 128 μV/K due to the variation of the mean distance between manganese ions "R" and the crystallite size "D". Polaron hopping parameters are obtained and reported in Table 4, the activation energy W can be described as:

$$W = W_D \text{ for } T < \frac{\theta_D}{4} \tag{9}$$

$$W = W_H + \left(\frac{W_D}{2}\right) \text{ for } T > \frac{\theta_D}{2} \tag{10}$$

where (W_H) is the polaron hopping energy and (W_D) is the disorder energy [54].

The polaron hopping energy (W_H) is related to the small polaron coupling constant (γ_p) by the following equation:

$$\gamma_P = \frac{2W_H}{h\nu_o} \tag{11}$$

γ_P represents the interaction between polaron and electron and ranged from 1.94 to 5.35 for the present samples. The density of state at the Fermi level $N(E_F)$ can be estimated from Eq. 12 while the polaron radius (r_p) can be calculated from R using Eq. 13 [55].

Table 4 Polaron hopping parameters

Milling time (h)	5	10	30	50
W_D (eV)	1.39E-02	8.21E-03	9.12E-03	1.32E-02
W_H (eV)	9.3E-02	5.83E-01	6.20E-01	5.47E-01
ε_P	119.99	362	287.7	249.27
r_p (nm)	0.26325	0.25115	0.25087	0.26082
J(eV)	0.171103	0.0144421	0.019817	0.024625
$N(E_F)$ (cm^{-3}) $\times 10^{21}$	8.57	1.68	1.585	1.59
γ_p	5.35753	1.949617	2.253459	2.610191
μ (cm^2 V^{-1} S^{-1}) $\times 10^{-6}$	1,912,925	0.015967	0.009014	0.1117

$$N(E_F) = 3/4\pi R^3 W \tag{12}$$

$$r_p = \left(\frac{\pi}{6}\right)^{\frac{1}{3}} \times \frac{R}{2} \tag{13}$$

The value of r_p used to obtain the hopping energy W_H using the following equations:

$$W_H = \left(\frac{e^2}{4\varepsilon_p}\right)\left(\frac{1}{r_p} - \frac{1}{R}\right) \tag{14}$$

$$\frac{1}{\varepsilon_p} = \frac{1}{\varepsilon_\infty} - \frac{1}{\varepsilon_s} \tag{15}$$

where: ε_p is the effective dielectric constant, ε_∞ is the static dielectric constant measured at high frequency (1 MHz) and ε_s is the optical dielectric constant. Another important parameter is the bandwidth of polaron associated with the electron wave function overlapping on the near sites (J), it can be calculated using the following relation [55].

$$J \approx e^3[N(E_F)/(\varepsilon_o\varepsilon_p)^3]^{1/2} \tag{16}$$

All the above parameters are needed to calculate the charge carrier mobility which found to be in the range $(1.685 \times 10^{-6}$ cm^2 V^{-1} s^{-1}–2.689×10^{-6} cm^2-V^{-1} s^{-1}). The values of hopping carrier mobility (μ) are given in Table 4 and can be obtained in the non-adiabatic hopping regime using the formula:

$$\mu = \left(\frac{eR^2}{kT}\right)\left(\frac{1}{h}\right)\left(\frac{\pi}{4W_HkT}\right)^{1/2} J^2\exp-\frac{W}{kT} \tag{17}$$

4 Conclusion

Bismuth manganese oxide $Bi_2Mn_4O_{10}$ is formed with a minority of secondary phases after milling time of 5 h and heat-treatment at 1073 K. The crystallite size of the prepared sample is varied from 47 to 102 nm after milling times of 1 h, 5 h, 10 h, 15 h, 30 h and 50 h. The values of the modulus of the Seebeck coefficient are obtained for prepared samples at 480 K, it varied with the values 277, 105, 69 and 45 µV/K at the milling times 5 h, 10 h, 30 h, and 50 h respectively. The ratio of the concentration of reduced transition metal (c) is varied from 0.15 to 0.26. The sample with 5 h of milling time owns the maximum value of |S| with a typical value of 277 µV/K, crystallite size of 58 nm and comparatively, the largest hopping carrier mobility (1.9129 cm^2 V^{-1} S^{-1}). According to the modulus values of Seebeck coefficient |S|, the sample at 5 h milling time can be used as a thermoelectric transducer. The number of manganese ions (N) for prepared samples is varied within the range $(1.502–1.736) \times 10^{22}/$cm^3 with separation average distance (R) varied from 0.622 to 0.653 nm. The temperature-dependent DC conductivity of the prepared samples is well-explained by Mott's small polaron theory, it is attributed to non-adiabatic hopping of small polaron (SPH) with a relatively-maximum value of 0.313 Sm^{-1} for the sample milled at 5 h.

Author contribution

The authors confirm contribution to the paper as Study conception: SAF, MI, AEH, MME-D. Data collection: SAF. Analysis and interpretation of results: SAF, AEH, MME-D. Draft manuscript preparation: SAF, MI, AEH, MME-D. All authors reviewed the results and approved the final version of the manuscript.

Funding

in cooperation with The Egyptian Knowledge Bank (EKB).

Research data policy and availability statement

We confirm that this work is original and has not been published elsewhere. In this work, all used data are available from our laboratories at which we prepared our samples. The used instruments and devices are mentioned in the manuscript clearly with the model number.

Declarations

Conflict of interest The authors declare that they have no known competing financial interests or personal relationships that could have appeared to influence the work reported in this paper.

Ethical approval We confirm that we took in consideration all the ethical rules in the attached research.

References

1. Z.S.D. Bochenek, Multiferroic materials for sensors, transducers and memory devices. Arch. Acoust. **33**, 243–260 (2008)

2. H.Z.Z. Song, K. Feng, H. Wang, X. Li, H. Zhang, $Bi_2Mn_4O_{10}$: a new mullite-type anode material for lithium-ion batteries. Dalton Trans. **47**, 7739–7746 (2018)

3. H. Wang, H. Zhang, K. Su, S. Huang, W. Tan, D. Huo, Structure, charge ordering, and magnetic properties of perovskite Sm0.5Ca0.5MnO3 manganite. J. Mater. Sci. Mater. Electron. **31**, 14421–14425 (2020)

4. I.O. Troyanchuk, D.D. Khalyavin, S.V. Trukhanov, H. Szymczak, A. Nabialek, Magnetotransport properties of the $Sm_{0.56}(Sr_{0.44-x}Mex)MnO_3$ (Me = Ba, Ca, Cd) perovskites. J. Phys. Condens. Matter **11**, 8913–8920 (1999)

5. A.A. Zatsiupa, L.A. Bashkirov, I.O. Troyanchuk, G.S. Petrov, A.I. Galyas, L.S. Lobanovsky, S.V. Trukhanov, Magnetization, magnetic susceptibility, effective magnetic moment of Fe^{3+} ions in $Bi_{25}FeO_{39}$ ferrite. J Sol. State Chem. **212**, 147–150 (2014)

6. S.V. Trukhanov, T.I. Zubar, V.A. Turchenko, A.V. Trukhanov, T. Kmjec, J. Kohout, L. Matzui, O. Yakovenko, D.A. Vinnik, A.Y. Starikov, V.E. Zhivulin, A.S.B. Sombra, D. Zhou, R.B. Jotania, C. Singh, A.V. Trukhanov, Exploration of crystal structure, magnetic and dielectric properties of titanium-barium hexaferrites. Mater. Sci. Eng. B **272**, 115345 (2021)

7. D.A. Vinnik, AYu. Starikov, V.E. Zhivulin, K.A. Astapovich, V.A. Turchenko, T.I. Zubar, S.V. Trukhanov, J. Kohout, T. Kmječ, O. Yakovenko, L. Matzui, A.S.B. Sombra, D. Zhou, R.B. Jotania, C. Singh, A.V. Trukhanov, Structure and magnetodielectric properties of titanium substituted barium hexaferrites. Ceram. Int. **47**, 17293–17306 (2021)

8. V. Turchenko, V.G. Kostishin, S. Trukhanov, F. Damay, M. Balasoiu, B. Bozzo, I. Fina, V.V. Burkhovetsky, S. Polosan, M.V. Zdorovets, A.L. Kozlovskiy, K.A. Astapovich, A. Trukhanov, Structural features, magnetic and ferroelectric properties of SrFe10.8In1.2O19 compound. Mater. Res. Bull. **138**, 1236 (2021)

9. A.V. Trukhanov, V.A. Turchenko, V.G. Kostishin, F. Damay, F. Porcher, N. Lupu, B. Bozzo, I. Fina, S. Polosan, M.V. Silibin, M.M. Salem, D.I. Tishkevich, S.V. Trukhanov, The origin of the dual ferroic properties in quasi-centrosymmetrical $SrFe_{12-x}In_xO_{19}$ hexaferrites. J. Alloy. Compd. **886**, 161249 (2021)

10. S.V. Trukhanov, Investigation of stability of ordered manganites. J. Exp. Theor. Phys. **101**, 513–520 (2005)

11. S.V. Trukhanov, I.O. Troyanchuk, V.V. Fedotova, V.A. Ryzhov, A. Maignan, D. Flahaut, H. Szymczak, R. Szymczak, Magnetic properties of the nonstoichiometric Sr-doped manganites. Phys. Stat. Solidi (b) **242**, 1123–1131 (2005)

12. D.V. Karpinsky, M.V. Silibin, S.V. Trukhanov, A.V. Trukhanov, A.L. Zhaludkevich, S.I. Latushka, D.V. Zhaludkevich, V.A. Khomchenko, D.O. Alikin, A.S. Abramov, T. Maniecki, W. Maniukiewicz, M. Wolff, V. Heitmann, A.L. Kholkin,

Peculiarities of the crystal structure evolution of BiFeO$_3$-BaTiO$_3$ ceramics across structural phase transitions. Nano-materials-Basel **10**, 801–812 (2020)

13. Z. Marinkovic, S.Z. Marinkovic, Z. Jaglic, M. Jagodic, L. Mancic, S. Bernik, A. Recnik, G. Brankovic, Structural and magnetic properties of nanocrystalline bismuth manganite obtained by mechanochemical synthesis. J Nanopart Res **13**, 3431–3439 (2011)

14. A. Thakur, N. Sharma, M. Bhatti, M. Sharma, A.V. Trukhanov, S.V. Trukhanov, L.V. Panina, K.A. Astapovich, P. Thakur, Synthesis of barium ferrite nanoparticles using rhizome extract of *Acorus Calamus*: characterization and its efficacy against different plant phytopathogenic fungi. Nano-Struct. Nano-Objects. **24**, 100599 (2020)

15. S.-Z. Hao, D. Zhou, C. Du, L.-X. Pang, C. Singh, S. Trukhanov, A. Trukhanov, A.S.B. Sombra, J. Varghese, Q. Li, X.-Q. Zhang, Temperature stable x(Na0.5Bi0.5)MoO4-(1−x)MoO3 composite ceramics with ultra-low sintering temperatures and low dielectric loss for dielectric resonator antenna applications. ACS Appl. Electron. Mater. **3**, 2286–2296 (2021)

16. Z. Branković, Z.M. Stanojević, L. Mančić, V. Vukotić, S. Bernik, G. Branković, Multiferroic bismuth manganite prepared by mechanochemical synthesis. J. Eur. Ceram. Soc. **30**(2), 277–281 (2010)

17. Z.H. Chi, H. Yang, S.M. Feng, F.Y. Li, R.C. Yu, C.Q. Jin, Room-temperature ferroelectric polarization in multiferroic BiMnO$_3$. J. Magnetism Magn. Mater. **310**(2, Part 2), 358–360 (2007)

18. Z.H. Chi, C.J. Xiao, S.M. Feng, F.Y. Li, C.Q. Jin, X.H. Wang, R.Z. Chen, L.T. Li, Manifestation of ferroelectromagnetism in multiferroic BiMnO$_3$. J. Appl. Phys. **98**(10), 103519 (2005)

19. M. Burianek, T.F. Krenzel, M. Schmittner, J. Schreuer, R.X. Fischer, M. Mühlberg, G. Nénert, H. Schneider, T.M. Gesing, Single crystal growth and characterization of mullite-type Bi$_2$Mn$_4$O$_{10}$. Int. J. Mater. Res. **103**(4), 449–455 (2012)

20. K. Ghosh, M.M. Murshed, T.M. Gesing, Synthesis and characterization of (Bi1−xRx)2Mn4O10: structural, spectroscopic and thermogravimetric analyses for R = Nd, Sm and Eu. J. Mater. Sci.: Mater. Electron. **54**(21), 13651–13659 (2019)

21. A.E. Hannora, Preparation of calcium manganese phosphate by mechanochemical synthesis of manganese and hydroxyapatite. J. Aust. Ceram. Soc. **55**(3), 807–815 (2019)

22. A.E. Hannora, S. Ataya, Structure and compression strength of hydroxyapatite/titania nanocomposites formed by high energy ball milling. J. Alloys Compd. **658**, 222–233 (2016)

23. A. Hannora, A. Mamaeva, Z. Mansurov, X-ray investigation of Ti-doped hydroxyapatite coating by mechanical alloying. Surf. Rev. Lett. **16**(5), 781–786 (2009)

24. S.N. Achary, O.D. Jayakumar, A.K. Tyagi, *4 - Multiferroic Materials* (Elsevier, London, 2012)

25. R.R.A.K. Kundu, V. Pralong, V. Gaignaert, B. Raveau, Magneto-transport and magneto-dielectric effects in Bi-based perovskite manganites. J. Mater. Chem **18**, 4280–4285 (2008)

26. A.A. Belik, J. Solid State Chem. **246**, 8–15 (2017)

27. M.H.S. Hanif, S. Riaz, S. Atiq, S.S. Hussain, S. Naseem, G. Murtaza, Structural, magnetic, dielectric and bonding properties of BiMnO$_3$ grown by co-precipitation technique. Results Phys. **7**, 3190–3195 (2017)

28. S. Zhang, S. Xu, H. Gao, Q. Lu, T. Lin, P. He, Characterization of multiple-filled skutterudites with high thermoelectric performance. J. Alloys Compd. **814**, 1572 (2020)

29. L.K.F. Ziegler, H. Gibhardt, T.M. Gesing, M.M. Murshed, O. Sobolev, A. Piovano, GötzEckold, characterization of multiferroic Bi$_2$Mn$_4$O$_{10}$ by dielectric and neutron spectroscopy. Phys. Status Solidi B **256**, 1800668 (2019)

30. J.T.A.Z.R. Kann, E.W. Hearn, S.U. Weber, K.D. Becker, H. Schneider, M.W. Lufaso, Mixed crystal formation and structural studies in the mullite-type system Bi$_2$Fe$_4$O$_9$–Bi$_2$Mn$_4$O$_{10}$. J. Solid State Chem. **185**, 62–71 (2012)

31. V. Naresh, S. Buddhudu, Studies on optical, dielectric and magnetic properties of Mn^{2+}, Fe^{3+}& Co^{2+} ions doped LFBCd glasses. Ferroelectrics (2012). https://doi.org/10.1080/00150193.2012.741987

32. L. Murawski, R. Barczyński, Dielectric relaxation in semiconducting oxide glasses. J. Non-crystalline Solids **196**, 275–279 (1996)

33. R.W.U.E.R.R. Heikes, *Thermoelectricity* (Interscience, New York, 1961)

34. J. Yang, T.B. Atwater, J.J. Xu, Improved cycling performance of bismuth-modified amorphous manganese oxides as cathodes for rechargeable lithium batteries. J. Power Sour. **139**(1), 274–278 (2005)

35. A. Leonarska, M. Kądziołka-Gaweł, A.Z. Szeremeta, R. Bujakiewicz-Korońska, A. Kalvane, A. Molak, Electric relaxation and Mn^{3+}/Mn^{4+} charge transfer in Fe-doped Bi$_{12}$MnO$_{20}$–BiMn$_2$O$_5$ structural self-composite. J. Mater. Sci. **52**(4), 2222–2231 (2017)

36. J. Zhan, C.-F. Xu, Y.-Y. Long, Q.-H. Li, Preparation and electrochemical performance of nitrogen-doped carbon-coated Bi$_2$Mn$_4$O$_{10}$ anode materials for lithium-ion batteries. Trans. Nonferrous Metals Soc. China **30**(8), 2188–2199 (2020)

37. J. Zhan, Y. Long, Synthesis of Bi$_2$Mn$_4$O$_{10}$ nanoparticles and its anode properties for LIB. Ceram. Int. **44**(12), 14891–14895 (2018)

38. S.V. Trukhanov, I.O. Troyanchuk, N.V. Pushkarev, H. Szymczak, Magnetic properties of anion-deficient

La1−xBaxMnO3−x/2 (0≤x≤0.30) manganites. J. Exp. Theor. Phys. **96**, 110–117 (2003)

39. S.V. Trukhanov, L.S. Lobanovski, M.V. Bushinsky, V.A. Khomchenko, N.V. Pushkarev, I.O. Tyoyanchuk, A. Maignan, D. Flahaut, H. Szymczak, R. Szymczak, Influence of oxygen vacancies on the magnetic and electrical properties of $La_{1-x}Sr_xMnO_{3-x/2}$ manganites. Eur. Phys. J. B **42**, 51–61 (2004)

40. S.V. Trukhanov, Magnetic and magnetotransport properties of $La_{1-x}Ba_xMnO_{3-x/2}$ perovskite manganites. J. Mat. Chem. **13**, 347–352 (2003)

41. S.V. Trukhanov, Peculiarities of the magnetic state in the system La0.70Sr0.30MnO3-γ ($0 \leq \gamma \leq 0.25$). J. Exp. Theor. Phys. **100**, 95–105 (2005)

42. M. Balaz, A. Zorkovska, J.S. Blazquez, N. Danue, Mechanochemistry of copper sulphides: phase interchanges during milling. J. Mater. Sci. **52**, 1–15 (2020)

43. E.I.K.I.A. Leonidov, M.V. Patrakeev, A.A. Markov, V.L. Kozhevnikov, Seebeck coefficient of $Ca_{1-x}Pr_xMnO_{3-\delta}$ paramagnetic manganites. Inorg. Mater. **53**, 583–588 (2017)

44. I.A. Abdel-Latif, Rare earth manganites and their applications. J. Phys. **3**, 15–31 (2012)

45. M.S.A.-A.A.M. Al-Syadi, H.M.A. Hassan, M.M. El-Desoky, Grain size effects on the transport properties of $Li_3V_2(PO_4)_3$ glass–ceramic nanocomposites for lithium cathode batteries. J Mater. Sci. **27**, 4074–4083 (2016)

46. D.A.H. Hirashima, T. Yoshida, Electrical conductivity of PbO-P_2O_5-V_2O_5 glasses. J. Am. Ceram. Soc. **68**, 486 (1985)

47. A.A.-H.A. Al-Shahrani, M.M. El-Desoky, Non-adiabatic small polaron hopping conduction in sodium borate tungstate glasses. Phys. Stat. Sol A **200**, 378–387 (2003)

48. N.F.M.I.G. Austin, Polarons in crystalline and non-crystalline materials. Adv. Phys. **18**(71), 41–102 (1969)

49. M.M. El-Desoky, M.M. Mostafa, M.S. Ayoub, M.A. Ahmed, Transport properties of Ba-doped $BiFeO_3$ multiferroic nanoparticles. J. Mater. Sci. **26**, 6793–6800 (2015)

50. N.F. Mott, Electrons in disordered structures. Adv. Phys. **16**, 49–144 (1967)

51. I.A. Leonidov, E.I. Konstantinova, M.V. Patrakeev, A.A. Markov, V.L. Kozhevnikov, Seebeck coefficient of $Ca_{1-x}Pr_xMnO_{3-\delta}$ paramagnetic manganites. Inorg. Mater. **53**(6), 583–588 (2017)

52. M.S. Dar, K.B. Akram, Evidence of variable range hopping (VRH) and exchange interaction in co-doped multiferroic $BiMnO_3$ nanoparticles. J. Supercond. Nov. Magn. **27**, 613–623 (2014)

53. A. Molak, D.K. Mahato, A.Z. Szeremeta, Synthesis and characterization of electrical features of bismuth manganite and bismuth ferrite: effects of doping in cationic and anionic sublattice: materials for applications. Prog. Cryst. Growth Charact. Mater. **64**(1), 1–22 (2018)

54. A. Ghosh, B.K. Chaudhuri, DC conductivity of V_2O_5-Bi_2O_3 glasses. J. Non-Cryst. Solids **83**(1), 151–161 (1986)

55. E.K.K. V. N. Bogomolov, YU. A. Firsov, Sov, Polaron nature of the current carriers in rutile TiO_2. Phys. Solid State **9**, 2502 (1968)